

## Durham Research Online

---

### Deposited in DRO:

12 July 2018

### Version of attached file:

Accepted Version

### Peer-review status of attached file:

Peer-reviewed

### Citation for published item:

van der Putten, Marieke A. and MacKenzie, Lewis E. and Davies, Andrew L. and Fernandez-Ramos, Javier and Desai, Roshni A. and Smith, Kenneth J. and Harvey, Andrew R. (2017) 'A multispectral microscope for in vivo oximetry of rat dorsal spinal cord vasculature.', *Physiological measurement.*, 38 (2). p. 205.

### Further information on publisher's website:

<https://doi.org/10.1088/1361-6579/aa5527>

### Publisher's copyright statement:

This is an author-created, un-copyedited version of an article accepted for publication/published in *Physiological Measurement*. IOP Publishing Ltd is not responsible for any errors or omissions in this version of the manuscript or any version derived from it. The Version of Record is available online at <https://doi.org/10.1088/1361-6579/aa5527>

### Additional information:

---

### Use policy

The full-text may be used and/or reproduced, and given to third parties in any format or medium, without prior permission or charge, for personal research or study, educational, or not-for-profit purposes provided that:

- a full bibliographic reference is made to the original source
- a [link](#) is made to the metadata record in DRO
- the full-text is not changed in any way

The full-text must not be sold in any format or medium without the formal permission of the copyright holders.

Please consult the [full DRO policy](#) for further details.



UNIVERSITY OF LEEDS

This is a repository copy of *A multispectral microscope for in vivo oximetry of rat dorsal spinal cord vasculature*.

White Rose Research Online URL for this paper:  
<http://eprints.whiterose.ac.uk/114252/>

Version: Accepted Version

---

**Article:**

van der Putten, MA, MacKenzie, LE orcid.org/0000-0002-8151-0525, Davies, AL et al. (4 more authors) (2017) A multispectral microscope for in vivo oximetry of rat dorsal spinal cord vasculature. *Physiological Measurement*, 38 (2). pp. 205-218. ISSN 0967-3334

<https://doi.org/10.1088/1361-6579/aa5527>

---

© 2017 Institute of Physics and Engineering in Medicine. This is an author produced version of a paper published in *Physiological Measurement*. Uploaded in accordance with the publisher's self-archiving policy.

**Reuse**

Unless indicated otherwise, fulltext items are protected by copyright with all rights reserved. The copyright exception in section 29 of the Copyright, Designs and Patents Act 1988 allows the making of a single copy solely for the purpose of non-commercial research or private study within the limits of fair dealing. The publisher or other rights-holder may allow further reproduction and re-use of this version - refer to the White Rose Research Online record for this item. Where records identify the publisher as the copyright holder, users can verify any specific terms of use on the publisher's website.

**Takedown**

If you consider content in White Rose Research Online to be in breach of UK law, please notify us by emailing [eprints@whiterose.ac.uk](mailto:eprints@whiterose.ac.uk) including the URL of the record and the reason for the withdrawal request.



[eprints@whiterose.ac.uk](mailto:eprints@whiterose.ac.uk)  
<https://eprints.whiterose.ac.uk/>

# A multispectral microscope for in vivo oximetry of rat dorsal spinal cord vasculature

Marieke A van der Putten<sup>1</sup>, Lewis E MacKenzie<sup>1</sup>, Andrew L Davies<sup>2</sup>, Javier Fernandez-Ramos<sup>1</sup>, [Roshni A Desai](#)<sup>2</sup>, [Kenneth J Smith](#)<sup>2</sup> and [Andrew R Harvey](#)<sup>1</sup>

<sup>1</sup> School of Physics and Astronomy, University of Glasgow, Glasgow, United Kingdom

<sup>2</sup> Department of Neuroinflammation, University College London Institute of Neurology, London, United Kingdom

Email: [Andy.Harvey@Glasgow.ac.uk](mailto:Andy.Harvey@Glasgow.ac.uk)

## Abstract

Quantification of blood oxygen saturation (SO<sub>2</sub>) in vivo is essential for understanding the pathogenesis of diseases in which hypoxia is thought to play a role, including inflammatory disorders such as multiple sclerosis (MS) and rheumatoid arthritis (RA). We describe a low-cost multispectral microscope and oximetry technique for calibration-free absolute oximetry of surgically exposed blood vessels in vivo. We imaged the vasculature of the dorsal spinal cord in healthy rats, and varied inspired oxygen (FiO<sub>2</sub>) in order to evaluate the sensitivity of the imaging system to changes in SO<sub>2</sub>. The venous SO<sub>2</sub> was calculated as  $67.8 \pm 10.4\%$  (average  $\pm$  standard deviation), increasing to  $83.1 \pm 11.6\%$  under hyperoxic conditions (100% FiO<sub>2</sub>) and returning to  $67.4 \pm 10.9\%$  for a second normoxic period; the venous SO<sub>2</sub> was  $50.9 \pm 15.5\%$  and  $29.2 \pm 24.6\%$  during subsequent hypoxic states (18% and 15% FiO<sub>2</sub> respectively). We discuss the design and performance of our multispectral imaging system, and the future scope for extending this oximetry technique to quantification of hypoxia in inflamed tissue.

Keywords: multispectral imaging, oximetry, spinal cord vasculature

## 1. Introduction

Tissue hypoxia is associated with inflammation in a range of diseases ([Eltzschig & Carmeliet, 2011](#)), including rheumatoid arthritis (RA) ([Taylor & Sivakumar, 2005](#)), and inflammation of the central nervous system such as occurs in multiple sclerosis (MS) ([Davies, et al., 2013](#)) ([Desai, et al., 2016](#)). Multispectral imaging (MSI) has become established as a method for oximetry with a diverse variety of in vivo applications, including non-invasive retinal oximetry ([Mordant, et al., 2011](#); [Choudhary, et al., 2013](#)), ocular microvascular oximetry ([MacKenzie, et al., 2016](#)), and investigation of tumour hypoxia in mouse models ([Sorg, et al., 2005](#)). The principle of MSI oximetry is based upon the oxygen-dependent optical absorption of haemoglobin - the dominant absorber of light in blood. Figure 1 shows the molar extinction coefficients of oxygenated and deoxygenated haemoglobin (values from [Prahl, 1999](#)).

Vascular oximetry using MSI involves estimation of the absorbance of blood vessels at various oxygen-insensitive (isosbestic) and oxygen-sensitive wavelengths. Optical density can be empirically related to SO<sub>2</sub>, provided there are known reference values for in vivo blood oxygenation (e.g. two-wavelength oximetry in the retina ([Beach, et al., 1999](#))). Unfortunately, for many applications there are no known reference values. Absolute calibration-free oximetry may be achieved however, by determining transmission of a vessel imaged at multiple wavebands, and fitting the measured

transmission values to a theoretical optical model. The model we employ here is based upon the modified Beer-Lambert law, and includes optical absorption, scattering, and other parameters. In this study we applied a multispectral oximetry algorithm which builds upon previous work by others (Schweitzer, et al., 1995) (Smith, et al., 2000). In addition, we introduce a contrast-reduction parameter to account for the effects of variations in thickness of tissue overlying blood vessels and neighbouring tissue (see Section 2.3).

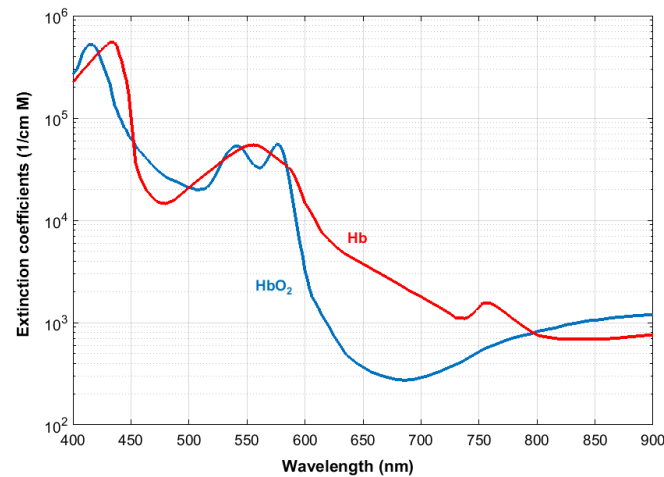


**Figure 1.** Molar extinction coefficients of oxygenated (HbO<sub>2</sub>) and deoxygenated haemoglobin (Hb) as a function of wavelength (Prahl, 1999).

To date, the SO<sub>2</sub> dynamics of the rat spinal cord dorsal veins have not been thoroughly investigated, with only a few limited studies conducted. Figley et al. (2013) reported use of a commercial two-wavelength photoacoustic tomography (PAT) imaging system to monitor a temporary decrease of the dorsal vein SO<sub>2</sub> in rats during hypoxia, however the method for calibration of the PAT device is not reported. Lesage et al. (2009) and Sharma et al. (2011) studied the use of optical imaging and non-imaging light-reflectance spectroscopy respectively, to monitor changes in concentration of oxyhaemoglobin in the rat spinal cord in response to electrical stimulation. Absolute SO<sub>2</sub> values were not reported, however.

Here we introduce a multispectral imaging system suitable for in vivo oximetry, and a complementary multispectral oximetry algorithm. The imaging system was designed and assembled using low cost, off-the-shelf optical components. We present results of measurement of venous SO<sub>2</sub> in the dorsal spinal cord vasculature of anaesthetised healthy control rats during normoxia (21% fraction of inspired oxygen [FiO<sub>2</sub>]), hyperoxia (100% FiO<sub>2</sub>), and hypoxia (18% and 15% FiO<sub>2</sub>). This approach could be applied to the in vivo study of a variety of experimental models in which hypoxia is thought to play a role.

## 2. Methods

### 2.1. Multispectral microscope

A schematic of the multispectral microscope is displayed in Figure 2. The microscope was designed such that the back focal length of the objective allowed sufficient working space for access to the exposed spinal cord of a rat under general anaesthesia. The microscope also enabled room for surgical equipment and was portable so as to be transferred between labs if necessary. A low-magnification, wide field-of-view system was implemented enabling oximetry of blood vessels across a range of diameters, and multispectral images between 546 nm and 600 nm were acquired.

84 Illumination was provided by a white LED (MWWHL3, Thorlabs) with a collimator lens of focal length  
 85 40.0 mm (COP-5A, Thorlabs). An additional lens (LA1509, Thorlabs,  $f = 100$  mm) served as a  
 86 condenser lens for the illumination path. The LED was controlled by a 4-channel driver (DC4100,  
 87 Thorlabs). A liquid crystal tuneable filter (LCTF) (VIS-7-HC-20, Varispec) provided electronically-  
 88 controllable spectral discrimination in 1 nm steps between 400 and 700 nm, with spectral full-width at  
 89 half maximum of 8 nm. Orthogonal polarisation imaging was used to null specular reflections from  
 90 blood vessels and ensure that only light which had diffused through tissue was imaged. This was  
 91 achieved by placing a linear polariser (LPVISE200-A, Thorlabs) in the illumination path arranged to  
 92 be orthogonal to the polarisation axis of the LCTF.

93 A single lens reflex (SLR) served as the microscope objective (AF Nikkor f/1.8,  $f = 50$  mm),  
 94 and was configured for finite conjugate imaging. The position of the SLR lens could be manually  
 95 translated along the z-axis for adjustment of focus. A digital SLR camera (D300s, Nikon) was used as  
 96 the detector.

97 Images were saved as 14-bit RGB NEF (RAW) format and converted to uncompressed  
 98 greyscale TIFF images for analysis. Greyscale conversion involved selecting either the red or the green  
 99 channel of the sensor and subtracting the respective dark current channel. The choice of red or green  
 100 channel was made for each waveband based on which provided higher SNR at that waveband; the red  
 101 channel was used for  $580 \leq \lambda \leq 600$  nm, and the green channel for  $546 \leq \lambda \leq 570$  nm. Image acquisition  
 102 rate was limited by the USB camera interface, which transferred RAW images at a rate of one image  
 103 every 7.5 seconds; thus a 6-band multispectral dataset was acquired in approximately 45 seconds total.  
 104 The SLR CMOS detector had 4288 x 2800 pixels and was 23.6 mm by 15.8 mm. The field of view of  
 105 this configuration was approximately 3.69 mm by 2.47 mm, giving a magnification factor of 6.4  
 106 corresponding to  $0.88 \mu\text{m}$  per pixel. Automated control of illumination, spectral filtering, and image  
 107 acquisition was achieved using a custom LabVIEW interface.

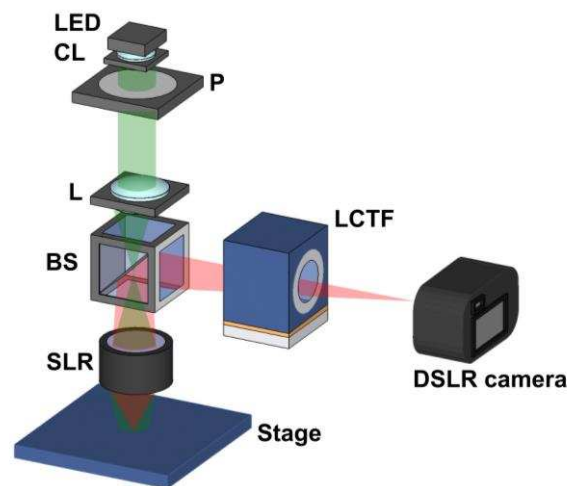


**Figure 2.** Schematic of multispectral microscope. LED: light emitting diode; CL: collimating lens; P: linear polariser; L: condenser lens; BS: beamsplitter; LCTF: liquid crystal tuneable filter; SLR lens is oriented with back focal plane towards the target. The illumination path is shown in green, and the imaging path in red.

## 2.2. Multispectral image processing and determination of optical transmission

Six wavebands were selected for imaging: 546, 560, 570, 584, 590 and 600 nm. Sensitivity to changes in  $\text{SO}_2$  was provided by the 560 nm, 590 nm and 600 nm wavebands. The 546 nm, 570 nm and 584 nm

wavebands were isosbestic, i.e. their absorptions are oxygen-insensitive (see Figure 1). These wavebands provided close to optimal transmission for oximetry in vessels approximately 100  $\mu\text{m}$  in diameter. Accurate oximetry is possible for  $0.1 < T < 0.7$  (Smith, 1999), where  $T$  is the proportional transmission of light propagated through the blood vessel. Wavelengths longer than 600 nm are unsuitable, as light of this wavelength is weakly absorbed by oxygenated haemoglobin, resulting in low contrast and hence sub-optimal transmission for accurate oximetry. Wavelengths below 546 nm had poor signal-to-noise ratio due to the low intensity of the LED and the low transmission of the LCTF at these wavelengths, and as such were also deemed unsuitable.

All image processing was implemented using custom algorithms in MATLAB. Images at each waveband were co-registered to form a 6-waveband multispectral data-cube. Vessels were tracked semi-automatically using user-defined control points. A vessel-profile fitting algorithm (see Figure 3) was used to estimate vessel diameter at each waveband at each point along the veins. Diameter estimation was based on the technique described by Fischer et al. (2000); this algorithm determines edges of the vessel as the points of greatest gradient in the 546 nm line profile. From this, the diameter of a vessel in pixels, and hence diameter in microns, could be determined. Transmission of vessels at each wavelength was then determined by a second vessel fitting algorithm. To estimate background intensity ( $I_o$ ), a linear fit (the red dashed line in Figure 3B) was applied to points of the line profile adjacent to the vessel. A second-order polynomial was fitted to the profile inside the vessel to estimate the intensity at the centre of the vessel ( $I$ ) (the black dashed line, Figure 3B). The transmission ( $T$ ) of the vessel was then calculated by  $T = \left(\frac{I}{I_o}\right)$ .

Only vessels meeting the following inclusion criteria were selected for tracking and oximetry analysis:

1. Vessels with diameter between 50 and 130  $\mu\text{m}$ .
2. Vessels producing a transverse line profile at least three times their diameter, and free of any adjacent vessels, to avoid systemic error in optical transmission calculation.
3. Vessels without taper - e.g. due to curvature around the spinal cord tissue.

Typically only one or two vessels per rat met these inclusion criteria.

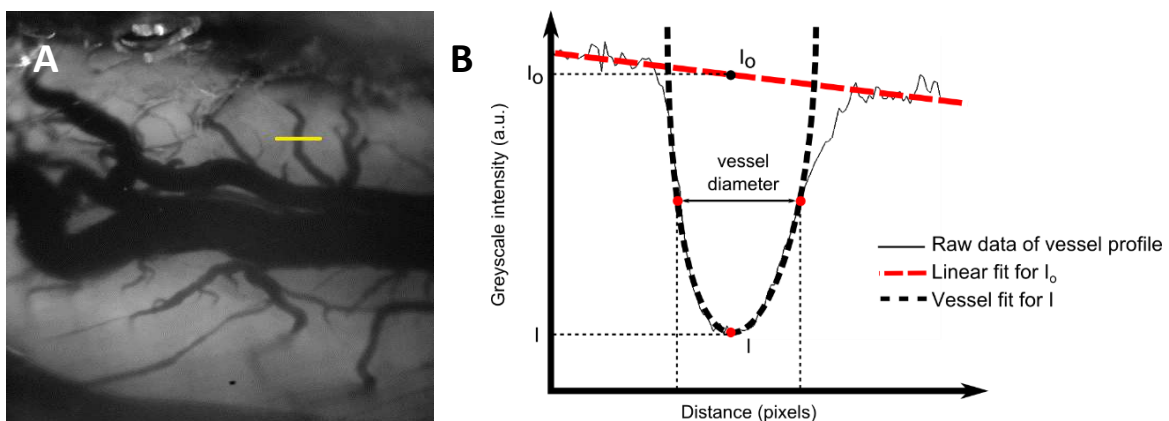


**Figure 3.** (A) Schematic of line profile along a spinal cord vessel – many such line profiles are taken along each vessel for analysis. (B) Illustration of vessel fitting algorithm used to determine vessel diameter and estimate transmission of light at each waveband.

### 2.3. Oximetry algorithm

A multispectral oximetry algorithm based on the work of [Smith et al. \(2000\)](#) was developed to estimate  $SO_2$  from transmission values of blood vessels. This algorithm fits a theoretical model of vessel transmission to experimentally measured transmission values, yielding an estimation of  $SO_2$ . The theoretical model predicts the wavelength-dependent transmission of a blood vessel of known diameter by accounting for blood oxygen saturation and incorporating empirical values for extinction and reduced scattering coefficients reported in the literature ([Prahl, 1999](#); [Bosschaart et al., 2014](#)). Further, we add an extra parameter – a contrast reduction parameter – to compensate for local variations in tissue thickness overlying vessels. This tissue tends to add a scattering component which reduces vessel contrast and hence transmission values, leading to incorrect estimation of  $SO_2$ . This section briefly describes how the model was derived.

From the Beer-Lambert law of optical transmission and absorption, we first defined the optical density (OD) of a blood vessel as:

$$OD = \log_{10}(T) = \varepsilon(\lambda)C_{HbT}d, \quad (1)$$

where  $T \left( T = \frac{I}{I_0} \right)$  is the experimentally measured transmission of a vessel as depicted in Fig. 3,  $d$  is the vessel diameter,  $C_{HbT}$  is the molar concentration of total haemoglobin, and  $\varepsilon(\lambda)$  is the effective optical extinction coefficient of haemoglobin;  $\varepsilon(\lambda)$  is dependent on both the oxygen saturation and wavelength-dependent molar extinction coefficients  $\varepsilon_{HbO_2}(\lambda)$  and  $\varepsilon_{Hb}(\lambda)$  of oxygenated and deoxygenated haemoglobin respectively. We used accepted values from the literature shown in Figure 1 ([Prahl, 1999](#)). These values are derived from human blood, but it has been shown that the difference between the absorption of light by haemoglobin in rats and humans is minimal ([Zijlstra, et al., 1994](#)). Defining  $c_1$  and  $c_2$  as proportional concentrations of oxygenated ( $HbO_2$ ) and deoxygenated (Hb) haemoglobin respectively, (1) is rewritten as

$$OD = (\varepsilon_{HbO_2}(\lambda) c_1 + \varepsilon_{Hb}(\lambda) c_2) d \quad (2)$$

where:  $c_1 + c_2 = C_{HbT}$ , so  $c_1 = C_{HbT}SO_2$  and  $c_2 = C_{HbT}(1 - SO_2)$ , and  $SO_2$  is the oxygen saturation; in other words, the proportion of oxygenated haemoglobin in the total solution of haemoglobin. It was also necessary to introduce a parameter to account for the optical scattering properties of blood. (2) is thus rewritten as:

$$OD = C_{HbT}d \left[ (\varepsilon_{HbO_2}(\lambda) - \varepsilon_{Hb}(\lambda))SO_2 + \varepsilon_{Hb}(\lambda) \right] + \mu'(\lambda)d \quad (3)$$

where the  $\mu'(\lambda)$  is the wavelength-dependent reduced scattering coefficient, which considers wavelength-dependent scattering ([Faber, et al., 2004](#)). By using compiled average values of scattering coefficients  $\mu(\lambda)$  and scattering anisotropy factors  $g(\lambda)$ , we determined these reduced scattering coefficients:  $\mu'(\lambda) = \mu(\lambda)(1 - g(\lambda))$  ([Bosschaart, et al., 2014](#)).

Two parameters,  $\alpha$  and  $\beta$ , are also introduced to account for the combination of single-pass transmission (light diffused through adjacent tissue and back-illuminating the vessel) and double-pass transmission (light transmitted directly through the vessel and scattered back from distal tissue). This concept is based on [Smith, et al., \(2000\)](#). Equation (3) is then rewritten in terms of transmission as:

$$T(\lambda) = \left( \alpha 10^{-\left( C_{HbT} d \left[ (\varepsilon_{HbO_2}(\lambda) - \varepsilon_{Hb}(\lambda))SO_2 + \varepsilon_{Hb}(\lambda) \right] + \mu'(\lambda)d \right)} + \beta 10^{-\left( 2C_{HbT} d \left[ (\varepsilon_{HbO_2}(\lambda) - \varepsilon_{Hb}(\lambda))SO_2 + \varepsilon_{Hb}(\lambda) \right] + 2\mu'(\lambda)d \right)} \right) \quad (4)$$



Finally, it was considered that various factors other than  $SO_2$  may alter the measured transmission values, such as scattering by overlying tissue. The imaging system itself may also introduce scattering and hence a loss of contrast. Contrast reduction was incorporated as an increase in greyscale intensity  $I_c$  of both the background and the vessel. Transmission was hence re-defined as  $T'(\lambda) = \left(\frac{I+I_c}{I_o+I_c}\right)$ . A contrast parameter  $K$  was introduced such that  $K = \frac{I_c}{I_o+I_c}$ . By substitution, this yields:  $T'(\lambda) = T(\lambda)(1 - K) + K$ . Applying this substitution to (4), a final model for transmission was derived:

$$T'(\lambda) = \left( \alpha 10^{-\left( C_{HbT}(\lambda)d \left[ \left( \epsilon_{HbO_2}(\lambda) - \epsilon_{Hb}(\lambda) \right) SO_2 + \epsilon_{Hb}(\lambda) \right] + \mu'(\lambda)d \right)} + \beta 10^{-\left( 2C_{HbT}(\lambda)d \left[ \left( \epsilon_{HbO_2}(\lambda) - \epsilon_{Hb}(\lambda) \right) SO_2 + \epsilon_{Hb}(\lambda) \right] + 2\mu'(\lambda)d \right)} \right) (1 - K) + K. \quad (5)$$

The experimentally measured transmissions are then fitted to (5) using a nonlinear least-squares fit. Additionally, vessel diameter was allowed to vary from the measured vessel diameter by  $\pm 5 \mu m$ . This yields estimated values of  $\alpha$ ,  $\beta$ ,  $K$ , and  $SO_2$ . The resulting fits were robust, with  $SO_2$  approximately constant along the vessel. Figure 4 presents an illustrative example of experimentally obtained transmissions along a blood vessel at all six wavebands, and the resulting  $SO_2$  values along the vessel, as produced by the algorithm.

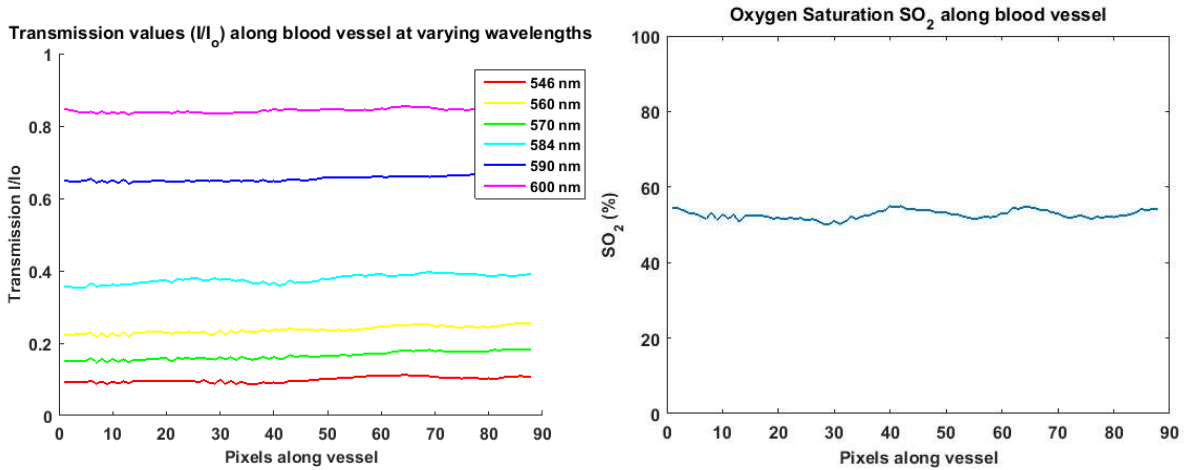


**Figure 4.** (A) Example of transmission profile along a tributary vessel. (B)  $SO_2$  estimated by the multispectral oximetry algorithm along the same vessel.

#### 2.4. In vivo imaging procedure

All procedures involving animals were carried out in accordance with the ARRIVE guidelines and the United Kingdom Home Office Animals (Scientific Procedures) Act 1986. Four female Dark Agouti rats (average weight 180 g) were used for the control validation study. A laminectomy was performed under 2% isoflurane anaesthesia in room air, and the dorsal aspect of vertebral segment L1 was removed to expose the cord for imaging. After surgery, the isoflurane was reduced to 1.5% for the remainder of the experiment, including all imaging. Motion due to animal heart-beat and breathing can provide a challenge for in vivo imaging, but surgical sutures were used to reduce loading of weight on the rat ribcage and the spinous process rostral to the exposed cord was clamped in place using a modified hemostatic clamp, minimising motion sufficiently for imaging. Similar strategies have been employed



in other studies which imaged the murine spinal cord ([Johannssen & Helmchen, 2010](#)), ([Vinegoni, et al., 2014](#)), ([Cadotte, et al., 2012](#)).

Arterial  $SO_2$  was monitored and recorded throughout the experiment using a pulse-oximeter collar (MouseOx, STARR Life). A homeothermic heating mat and rectal temperature probe maintained the rectal temperature at  $37^\circ C$ . For each rat, image exposure time for each waveband was optimised to ensure sufficient exposure and to avoid image saturation.

Assessing changes in  $SO_2$  due to changes in  $FiO_2$  is an effective way of testing the sensitivity of the oximetry technique. To assess response to changes in  $FiO_2$  in healthy rats,  $FiO_2$  was varied sequentially, with three full multispectral datasets acquired at each stage of the experiment. The following sequence was used: baseline normoxia (21%  $FiO_2$  for 10 minutes), hyperoxia (100%  $FiO_2$  for 10 minutes), return to normoxia (normoxia 2, 21%  $FiO_2$  for 5 minutes), then incrementally decreasing  $FiO_2$  to induce progressive hypoxia (hypoxia 1, 18% and hypoxia 2, 15%; 5 minutes each). Similar protocols have been used in previous oximetry studies ([MacKenzie, et al., 2016](#)), and have been shown to produce a sequence of  $SO_2$  changes that is clearly distinct from normal physiological variation.

### 3. Results

#### 3.1. Images acquired

Multispectral images were successfully acquired at baseline normoxia 1, hyperoxia, normoxia 2, and hypoxia 1 for all four rats. Rat 1 died before the hypoxia 2 oxygenation state (15%  $FiO_2$ ), and thus hypoxia 2 data are omitted for this rat. Representative multispectral images of rat spinal cord dorsal vein are shown in Figure 5. The large dorsal vein lies on the dorsal surface of the spinal cord along the rostral-caudal axis, with numerous smaller tributary veins. The large dorsal vein is too absorbing for accurate oximetry, so tributary veins were analysed, provided they met the inclusion criteria described in Section 2.2.

#### 3.2. Response to changes in $FiO_2$

Average venous  $SO_2$  values are shown in Figure 6. Corresponding arterial values, as measured by the pulse oximeter, are also presented. As expected, average baseline venous  $SO_2$  increased during hyperoxia ( $67.8 \pm 10.4\%$  [mean  $\pm$  standard deviation] increasing to  $83.1 \pm 11.6\%$ ), and returned to baseline values during the second state of normoxia ( $67.4 \pm 10.9\%$ ) and further decreased during subsequent hypoxic periods ( $50.9 \pm 15.5\%$  and  $29.2 \pm 24.6\%$  respectively). The differences in average  $SO_2$  between consecutive oxygenation states were all statistically significant ( $p < 0.05$ , pairwise t-test), with changes between normoxia 1 and hyperoxia, hyperoxia and normoxia 2, and normoxia 2 and hypoxia 1 all highly significant ( $p < 0.01$ ). The normoxia baseline  $SO_2$  values and changes due to  $FiO_2$  interventions are physiologically plausible (normal venous  $SO_2$  is typically  $\sim 70\%$ ), helping to validate our multispectral oximetry algorithm. The results for venous  $SO_2$  for all individual animals are shown in Figure 7 and Table 1. Vessel diameter measurements for all animals are summarised in Table 2, including results of a pairwise t-test between all diameter values at consecutive oxygenation states – which suggested no relationship between measured  $SO_2$  and vessel calibre.

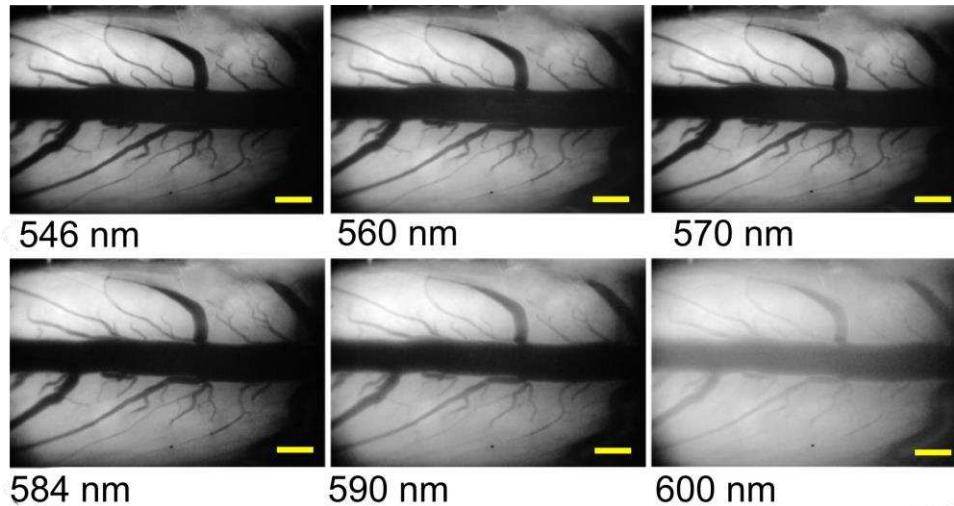


**Figure 5.** Multispectral images of spinal cord dorsal vein vasculature in a single rat. The main dorsal vein lies on the dorsal surface of the spinal cord, with numerous tributary veins joining the larger vessel. The scale bars represent 500  $\mu\text{m}$ .

### 3.3. Repeatability and inter-animal variability of measurements

Repeatability of measurements was assessed by performing three measurements of  $\text{SO}_2$  at baseline normoxia for each individual rat, where physiological variations are expected to be minimal. The average standard deviation of repeat measurements across all animals was  $\pm 2.28\%$   $\text{SO}_2$ . This deviation is much lower than changes in  $\text{SO}_2$  observed due to variation of  $\text{FiO}_2$  – which was above 15% between normoxia and hyperoxia, and even greater for changes between normoxia and subsequent states of hypoxia. This indicated sufficient repeatability over individual vessels for ascertaining changes in  $\text{SO}_2$ .

The changes in venous  $\text{SO}_2$  observed throughout the experiment were strongly correlated with changes in arterial  $\text{SO}_2$ , as measured by the pulse oximeter. The calculated Pearson correlation coefficients  $r$  were 0.74, 0.79, 0.87, and 0.88 for each rat respectively ( $p < 0.01$ ). There was, however, considerable variation in average baseline venous  $\text{SO}_2$  between individual rats, ranging from 53% to 78% at normoxia. We did not find a correlation between this variation in venous  $\text{SO}_2$  and the baseline arterial  $\text{SO}_2$  values. Some physiological variation is expected between rats due to potential differences in depth of anaesthesia and the temperature of the exposed spinal cord (despite maintenance of rectal temperature), both of which may affect venous oxygen saturation.

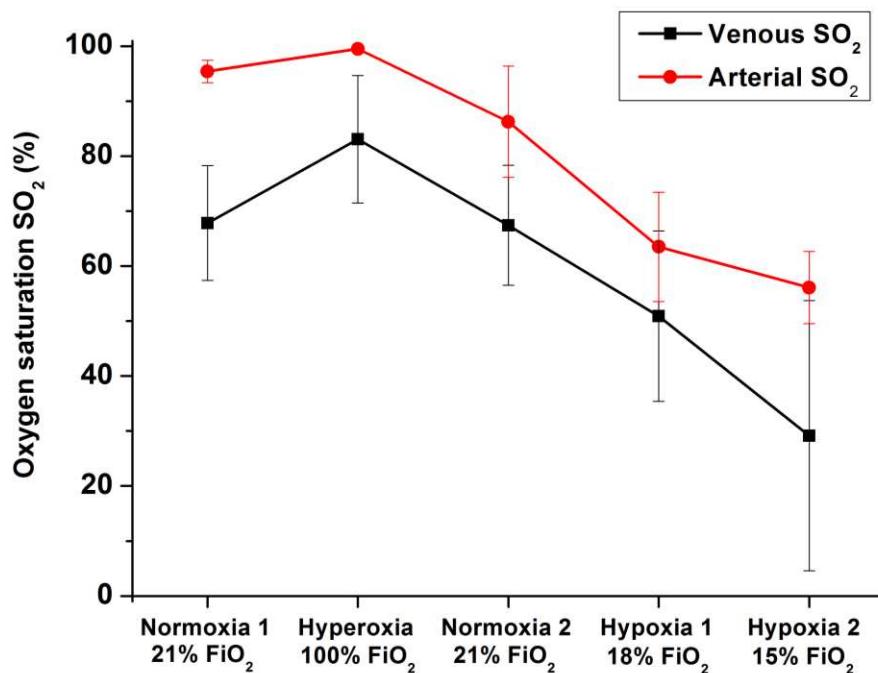


**Figure 6.** Average venous SO<sub>2</sub> across all animals with variation in FiO<sub>2</sub>. Corresponding average pulse oximeter data are also presented. Error bars represent the standard deviation of the average values of each individual rat.

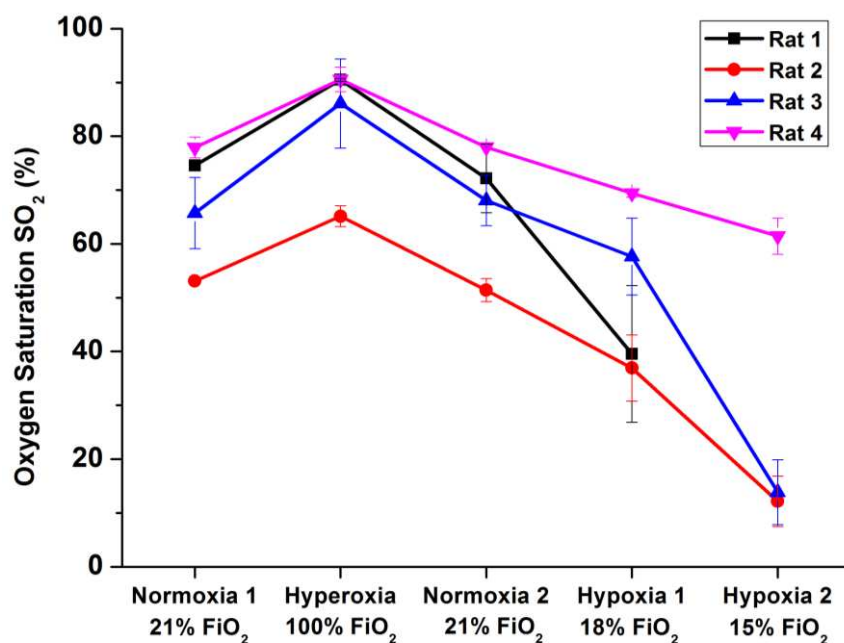


**Figure 7.** Variation in SO<sub>2</sub> with FiO<sub>2</sub> for each control rat. Results are the average value for each rat  $\pm$  standard deviation.

**Table 1.** SO<sub>2</sub> measurements for individual control rats.

Average rat SO <sub>2</sub> ± standard deviation (%)						Change (p-value)
	Rat 1	Rat 2	Rat 3	Rat 4	Average	
<b>Normoxia 1</b> (21% FiO <sub>2</sub> )	74.6 ± 0.1	53.1 ± 0.5	65.8 ± 6.6	77.9 ± 1.9	67.8 ± 10.4	n/a
<b>Hyperoxia</b> (100% FiO <sub>2</sub> )	90.5 ± 0.3	65.2 ± 1.93	86.1 ± 8.3	90.6 ± 2.3	83.1 ± 11.6	<0.01
<b>Normoxia 2</b> (21% FiO <sub>2</sub> )	72.2 ± 6.4	51.4 ± 2.1	68.1 ± 4.7	78.0 ± 0.2	67.4 ± 10.9	<0.01
<b>Hypoxia 1</b> (18% FiO <sub>2</sub> )	39.6 ± 12.7	36.9 ± 6.2	57.7 ± 7.2	69.4 ± 0.7	50.9 ± 15.5	<0.01
<b>Hypoxia 2</b> (15% FiO <sub>2</sub> )	N/A	12.2 ± 4.7	13.8 ± 6.00	61.5 ± 3.4	29.2 ± 24.6	<0.05

**Table 2.** Vessel diameter measurements throughout the experiment.

Average vessel diameter ± standard deviation (µm)					Change (p-value)
	Rat 1	Rat 2	Rat 3	Rat 4	
<b>Normoxia 1</b> (21% FiO <sub>2</sub> )	104.5 ± 0.9	87.7 ± 0.6	59.5 ± 1.4	100.5 ± 1.1	n/a
<b>Hyperoxia</b> (100% FiO <sub>2</sub> )	108.1 ± 0.6	89.8 ± 1.8	59.3 ± 1.4	103.0 ± 3.3	0.89
<b>Normoxia 2</b> (21% FiO <sub>2</sub> )	105.5 ± 1.6	87.6 ± 0.7	57.9 ± 5.00	97.7 ± 1.3	0.81
<b>Hypoxia 1</b> (18% FiO <sub>2</sub> )	107.0 ± 0.7	86.0 ± 0.7	60.8 ± 1.7	99.4 ± 1.4	0.88
<b>Hypoxia 2</b> (15% FiO <sub>2</sub> )	N/A	81.7 ± 0.6	61.7 ± 1.3	99.3 ± 0.2	0.34

## 4. Discussion

### 4.1. Performance of the multispectral microscope

The multispectral microscope provided images of the dorsal vasculature of the rat spinal cord with sufficient magnification and spectral contrast for oximetry of vessels approximately 50 to 130 µm in diameter. Data acquisition was fully automated using a LabVIEW interface to minimise acquisition time and potential human error. Further, the multispectral microscope was assembled with off-the-shelf components, making it a relatively simple and cost-effective device. Using a digital SLR CMOS detector was cost-efficient in comparison with scientific CCD or CMOS detectors, and provided sufficient performance. Further reduction in cost could be achieved by replacing the LCTF with a bank of bandpass filters. The LCTF has the advantage of rapid tuning and adaptability, but LCTF transmission is low and it is the most costly component of the microscope. A computer-controlled filter

wheel would result in slower switching between wavebands, but this would be compensated by shorter integration times afforded by higher optical throughput.

Integration time was less than 1 second for all wavelengths; for the 584 nm, 590 nm and 600 nm wavebands where LCTF transmission is higher, the integration time was as low as 100 ms. Multispectral dataset acquisition rate was limited, however, by the LabVIEW SLR camera control toolbox used (LabVIEW Camera Control for Nikon SLR, Ackerman Automation). The resulting data-transfer speed was limited by the USB 2.0 capability of the SLR camera, which limited image acquisition to once every 7.5 seconds. This resulted in an acquisition time of approximately 45 seconds for a multispectral dataset. Acquisition time could be greatly improved in future by using a SLR camera with USB 3.0 capability.

#### 4.2. Performance and validation of oximetry algorithm for in vivo imaging

Our oximetry algorithm is based on an algorithm published by Smith et al. (2000) and we have used empirical values of scattering coefficient, anisotropy factor, and extinction coefficients of oxygenated and deoxygenated haemoglobin to provide a transmission-based model for estimation of  $SO_2$ . A contrast-reduction parameter was also added to compensate for the effects of any tissue overlying blood vessels.

Vessel diameter may influence other parameters in our algorithm, such as degree of optical scattering and optical path length of light. In two-wavelength oximetry, for example, it has been reported that large retinal veins are estimated to have a lower blood oxygen saturation than smaller veins (Hammer, et al., 2008), but this may be a vein-diameter dependent calibration artefact in two-wavelength oximetry. We found that fluctuations in diameter for a given vessel between consecutive oxygenation states were not statistically significant (see Table 2).

It is clear from measurement that our oximetry analysis provides physiologically plausible values for  $SO_2$ , is sensitive to changes in  $SO_2$ , and is insensitive to vessel diameter. However, highly accurate validation of our oximetry algorithm remains challenging in vivo. Whilst the correlations with arterial pulse oximeter data go some way towards explaining the variability in baseline venous  $SO_2$ , verifying the absolute values produced by our technique is difficult. An option for an in vitro validation study is to use whole ex vivo blood in transparent fluorinated ethylene propylene (FEP) capillaries, placed on a diffuse white reflective background material such as Spectralon<sup>TM</sup>. In vitro validation requires variation of  $SO_2$  in blood, generally achieved by addition of measured quantities of sodium dithionite (Briely-Sabo & Bjornerud, 2000). However, sodium dithionite alters the osmolarity of blood which affects optical properties, including scattering coefficients and anisotropy (Friebel, et al., 2010). The development of a more realistic phantom and an alternative method to artificially deoxygenate whole blood, such as the use of nitrogen gas, would be beneficial and will be considered for future studies (Ghassemi, et al., 2015) (Denninghoff & Smith, 2000).

Many tributary vessels present in the images were too small ( $< 50 \mu m$ ) to meet our inclusion criteria: such vessels absorb light too weakly for accurate oximetry with the wavelengths used. To enable analysis of smaller vessels, blue wavelengths (at which absorption is higher) could be incorporated into the imaging scheme, providing sufficient contrast for accurate determination of transmission profiles. This would increase the number of veins appropriate for analysis.

## 5. Conclusions

We have developed a cost-effective multispectral microscope to enable in vivo, calibration-free, absolute oximetry of surgically-exposed dorsal veins of healthy rats.  $SO_2$  and vessel diameters of tributary dorsal veins were calculated for a range of inspired oxygen concentrations. This algorithm

yielded physiologically plausible values for  $\text{SO}_2$  for each rat during normoxia, hyperoxia and graded hypoxia, with  $\text{SO}_2$  changing as expected. Further, these results correlated significantly with corresponding arterial  $\text{SO}_2$  values as determined by pulse oximetry.

The imaging system and oximetry technique provides sufficient sensitivity to  $\text{SO}_2$  such that it may be applied to the study of a variety of disease models where hypoxia may be a factor. The preliminary results presented in this paper suggest that any significant changes in  $\text{SO}_2$  related to specific pathological changes will be quantifiable, and it is hoped that future studies using this technique will provide a deeper understanding of disease pathology. The oximetry algorithm developed may be easily extended to a wide range of other applications in future where localised  $\text{SO}_2$  measurement is required in vivo, such as oximetry in rodent models of multiple sclerosis, rheumatoid arthritis and non-invasive retinal oximetry in humans.

### Acknowledgment

This work was funded by the University of Glasgow Sensors Initiative and the Lord Kelvin Adam Smith scholarship programme.

### References

- Beach, J. et al., 1999. Oximetry of retinal vessels by dual-wavelength imaging: calibration and influence of pigmentation. *Journal of Applied Physiology*, pp. 748-758.
- Boschaart, N. et al., 2014. A literature review and novel theoretical approach on the optical properties of whole blood. *Lasers in Medical Science*, Volume 29, pp. 453-479.
- Briely-Sabo, K. & Bjornerud, A., 2000. Accurate de-oxygenation of ex vivo whole blood using sodium Dithionite. *Proc. Intl. Sot. Mag. Reson. Med*, Volume 8, p. 2025.
- Cadotte, D. W. et al., 2012. Speckle variance optical coherence tomography of the rodent spinal cord: in vivo feasibility. *Biomedical Optics Express*, 3(5), pp. 911-919.
- Choudhary, T. R. et al., 2013. Assessment of acute mild hypoxia on retinal oxygen saturation using snapshot retinal oximetry. *Investigative ophthalmology & visual science*, 54(12), pp. 7538-43.
- Davies, A. L. et al., 2013. Neurological Deficits Caused by Tissue Hypoxia in neuroinflammatory disease. *Annals of Neurology*, 74(6), pp. 815-825.
- Denninghoff, K. & Smith, M., 2000. Optical model of the blood in large retinal vessels. *Journal of Biomedical Optics*, 5(4), pp. 371-374.
- Desai, R. et al., 2016. Cause and prevention of demyelination in a model multiple sclerosis lesion. *Annals of Neurology*, 79(4), pp. 591-604.
- Eltzschig, H. & Carmeliet, P., 2011. Hypoxia and Inflammation. *N Engl J Med*, Volume 364, pp. 656-65.
- Faber, D. J. et al., 2004. Oxygen Saturation-Dependent Absorption and Scattering of Blood. *Physics Review Letters*, 93(2).
- Figley, S. A. et al., 2013. A Spinal Cord Window Chamber Model for In Vivo Longitudinal Multimodal Optical and Acoustic Imaging in a Murine Model. *PLOS one*, 8(3).

- Friebel, M., Helfmann, J. & Meinke, M. C., 2010. Influence of osmolarity on the optical properties of human erythrocytes. *J. Biomed. Opt.*, 15(5).
- Ghassemi, P. et al., 2015. Rapid prototyping of biomimetic vascular phantoms for hyperspectral reflectance imaging. *Journal of Biomedical Optics*, 20(12).
- Hammer, M., Vilser, W., Riemer, T. & Schweitzer, D., 2008. Retinal vessel oximetry-calibration, compensation for vessel diameter and fundus pigmentation, and reproducibility. *J. Biomed Opt.*, 13(5).
- Johannssen, H. C. & Helmchen, F., 2010. In vivo Ca<sup>2+</sup> imaging of dorsal horn neuronal populations in mouse spinal cord. *The Journal of physiology*, 588(18), pp. 3397-3402.
- Lesage, F., Brieb, N., Dubeaub, S. & Beaumont, E., 2009. Optical imaging of vascular and metabolic responses in the lumbar spinal cord after T10 transection in rats. *Neuroscience letters*, 454(1), pp. 105-109.
- MacKenzie, L., Choudhary, T., McNaught, A. & Harvey, A., 2016. In vivo oximetry of human bulbar conjunctival and episcleral microvasculature using snapshot multispectral imaging. *Experimental Eye Research*.
- Mordant, D. et al., 2011. Spectral imaging of the retina. *Eye*, Volume 25, pp. 309-320.
- Prahl, S., 1999. Optical Absorption of Hemoglobin. Oregon Medical Laser Center, <http://omlc.org/spectra/hemoglobin/index.html>.
- Schweitzer, D. et al., 1995. Calibration-free measurement of the oxygen saturation in retinal vessels of men. *Proc. SPIE, Ophthalmic Technologies V*, 2393(210).
- Sharma, V. et al., 2011. Quantification of light reflectance spectroscopy and its application: Determination of hemodynamics on the rat spinal cord and brain induced by electrical stimulation. *NeuroImage*, 56(3), pp. 1316-1328.
- Smith, M., 1999. Optimum wavelength combinations for retinal vessel oximetry. *Applied optics*, 38(1), pp. 258-67.
- Smith, M. H., Denninghoff, K. R., Lompad, A. & Hillman, a. L. W., 2000. Effect of multiple light paths on retinal vessel oximetry. *Applied Optics*, 39(7), pp. 1183-93.
- Sorg, B. S. et al., 2005. Hyperspectral imaging of hemoglobin saturation in tumor microvasculature and tumor hypoxia development. *Journal of biomedical optics*, 10(4).
- Taylor, P. C. & Sivakumar, B., 2005. Hypoxia and angiogenesis in rheumatoid arthritis. *Current opinion in rheumatology*, Volume 17, pp. 293-298.
- Vinegoni, C., Lee, S., Feruglio, P. F. & Weissleder, R., 2014. Advanced Motion Compensation Methods for Intravital Optical Microscopy. *IEEE Journal of Selected Topics in Quantum Electronics*, 20(2).
- Zijlstra, W., Buursmaa, A., Falke, H. & Catsburg, J., 1994. Spectrophotometry of hemoglobin: absorption spectra of rat oxyhemoglobin, deoxyhemoglobin, carboxyhemoglobin, and methemoglobin. *Comp. Biochem. Physiol.*, 107B(1), pp. 161-166.